14.3 EDDY CORRELATION MEASUREMENTS OF WAVE-INDUCED STRESS USING INSTRUMENTS MOUNTED ON A WAVE FOLLOWER

Cor Jacobs[*], *Wiebe Oost, Cor van Oort and Ed Worrell*
Royal Netherlands Meteorological Institute (KNMI), The Netherlands

1. INTRODUCTION

Modulation of velocity disturbances by water waves induces an additional stress component over the ocean. As a result, the total momentum transport in the Atmospheric Surface Layer (ASL) at sea, τ_0, is composed of the turbulent transport, τ_t, the viscous transport, τ_v, and the wave-induced momentum flux, τ_w:

$$\tau_0 = \tau_v(z) + \tau_w(z) + \tau_t(z) \equiv \rho_a u_*^2 \qquad (1)$$

where z is height, ρ_a is the density of the air and u_* is the friction velocity. The ratio $\tau_w(0)/(\rho_a u_*^2)$, indicating the fraction of the momentum flux at the surface that is supported by form drag, is called the coupling parameter (Makin and Kudryavtsev, 1999). This parameter has been used to model the roughness of the sea surface (see, e.g., Bye *et al*., 2001, for a discussion of this subject). We will ignore the viscous stress τ_v, as it is only important in the immediate proximity of the surface, where τ_t, vanishes. On the other hand, τ_t becomes fully dominant somewhat further away from the surface. The layer between these two extremes is often called the Wave Boundary Layer (WBL), which may be defined as the layer with a significant influence of the waves on the turbulence in the ASL. The height of the WBL is then taken to be the level where τ_w vanishes. It is generally believed that this height is, typically, only 1-2 wave heights (Grachev and Fairall, 2001). Thus, observing the turbulent characteristics of the WBL requires measurements very close to the surface, preferably below the level of the wave crests. Due to the tremendous difficulties to perform such measurements at sea only little information on the WBL is available from field measurements. Recent attempts to determine the turbulent characteristics of the WBL from observations (e.g., Hare *et al*., 1997, Wilczak *et al*., 1999) have been restricted to heights above the level of the highest wave crests. Here, we report on eddy correlation (EC) measurements of the momentum flux well below the level of the wave crests, using specialized pressure anemometers mounted on a wave follower.

As in Hristov *et al*. (1999) our approach to observe the wave-induced stress utilizes a definition of $\tau_w(z)$ that can be derived from the Navier-Stokes equation in the ASL, by taking into account wave coherent influences on the flow. Variable a may be decomposed into a mean ($\bar{a}$), turbulent (a') and wave-induced ($\tilde{a}$) part:

$$a = \bar{a} + \tilde{a} + a' \qquad (2)$$

Applying the averaging rules described in Finnigan *et al*. (1984), it can be shown that (*cf*. Hare *et al*., 1997):

$$\tau_w = \rho_a(\overline{\tilde{u}\tilde{w}} + \overline{\tilde{v}\tilde{w}}) \qquad (3)$$

where u and v are, respectively, the streamwise and lateral velocity, and w is the vertical velocity.

A more classical approach is to relate τ_w to the correlation between wave-induced pressure variations and the wave slope. Various attempts to determine this correlation using wave-following and other systems in the laboratory or at sea are reviewed by Young (1999). This approach was not attempted here and will be deferred to a future experiment.

2. OBSERVATIONS

The wave follower (WF) used in this study is schematically depicted in Figure 1. It is designed to follow surface waves with frequencies of 1 Hz or less. Our WF consists of a tall vertical pole that moves up and down by means of a strong servo-electromotor. A water level sensor at the lower end of the pole detects the position of the system relative to the instantaneous water surface. The signals from this sensor are processed by a digital motion control system in a 60 Hz control cycle. A Kalman filter, implemented on the servo system, predicts the position of the water surface one timestep ahead, using the "error" from the water level sensor, that is, the deviation of the water surface from the center of the sensor. This "error" is then minimized by moving the pole towards the predicted position. In this way, the system remains at a fixed distance from the water surface (relative to waves with frequencies < 1Hz).

The WF is attached to a special boom, deployed at Meetpost Noordwijk (MPN), a stable research platform in the North Sea 9 km off the Dutch coast in water with an average depth of 18m. The outrigger keeps the pole in an accurately vertical position. The boom is attached to the platform some 6m above the mean sea level, well below the deckhouse of MPN. It is pointing towards the North, and extends about 12 m in front of the platform. This configuration allows meaningful observations with the WF to be made at wind directions between Southwest and Northeast, over North (220°-360°/0°-45°). For other wind

[*]*Corresponding author address: Cor M.J. Jacobs, KNMI, P.O. Box 201, 3730 AE, De Bilt, The Netherlands; e-mail: cor.jacobs@knmi.nl*

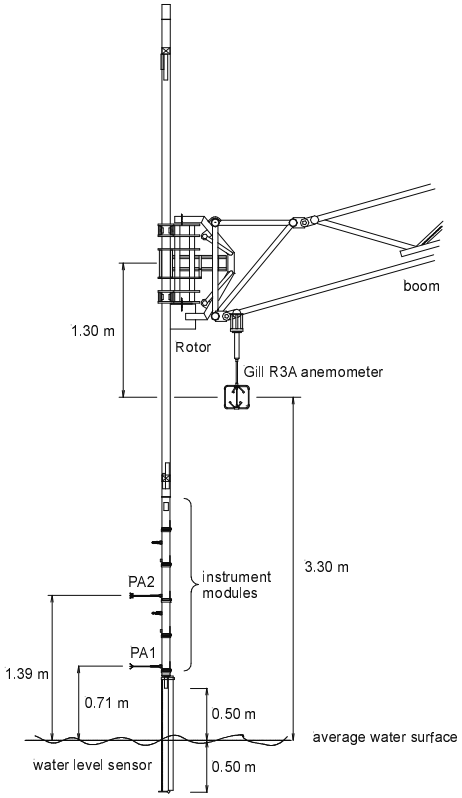

Figure 1. Schematic illustration of the wave follower. See main text for a further explanation.

directions, flow distortion by the platform will induce irrecoverable errors. In between runs, the instruments may be aimed in the mean wind direction by turning the full WF, using a rotor fixed at the end of the outrigger.

The WF motion is strictly vertical, so that no platform-related pitch-and-roll corrections to the turbulence data are required. The delay in the wave following motion is small enough to ensure measurements in an almost perfect wave-following co-ordinate system. The distortion of the local wave field is minimal thanks to the small area in contact with the water surface. Another favorable characteristic is the limited diameter (7.6 cm) of the instrument modules that carry the sensors, which minimizes flow distortion.

Micrometeorological instruments are mounted on the WF using a system of interchangeable tubular elements. Each of these modules has one or two positions where specific instruments can be attached. External cables are avoided because connectors integrated in the modules allow signals from the internal processing boards to be transferred from one module to the other, and to the signal cables within the main pole. At present, the wave follower can carry up to five modules.

For EC measurements on the WF we deploy a specialized type of the pressure anemometers (PA) developed at KNMI. The averaging path of the PA is only 4-5 cm. This is smaller than that of most wind sensors that are commercially available to date, and it allows measurements close to the surface without losing a significant part of the contribution of small turbulent eddies to the flux. Because the PA is kept under a slight overpressure, the sensor is self-cleaning. Dried air is provided to the PA's by means of metal conduits integrated in the instrument modules and the main pole. This construction avoids pumping effects due to WF motions. A full description of the PA and its properties can be found in Oost *et al*. (1991).

The measurements described here were performed with PA's mounted at 0.71 (henceforth: PA1) and 1.39 m (PA2) above the actual water surface, respectively. These observations were supported by measurements with a Gill R3A sonic anemometer, mounted on the WF boom at a fixed height of about 3.30 m above the average water level (GS). Before the experiment, all instruments were carefully calibrated in a wind tunnel, using a procedure described by Kraan and Oost (1988). During the calibration, the PA's are attached to the pertinent WF instrument modules to compensate for flow distortion effects due to these modules.

A WF field experiment was performed at MPN in November 2001. We were able to collect 183 20-minute data runs. The sampling frequency was 40 Hz for all instruments. Data on the general meteorological and oceanographic conditions are obtained from the operational observations at MPN. These data include (directional) wave spectra, significant and maximum wave height (H_s and H_{max}), peak frequency and phase speed at the peak frequency (C_p).

3. RESULTS

Here, we report a first analysis of our data. Later reports will give more detailed analyses.

The wind speed at a height of 10 m (U_{10}) and u_*, derived from the GS, are shown in Figure 2a, along with C_p. In most cases, $C_p > U_{10}$, but we note that many wave spectra were double-peaked, indicating mixed seas with swell and wind sea. C_p/U_{10} ranged between 0.78 and 4.3, while C_p/u_* ranged between 20 and 120. In our further analysis, we will use the latter wave age parameter. Also shown are H_s and H_{max} from the directional waverider near MPN, along with the levels of PA1 and PA2 (Fig. 2b). It can be seen that it was possible to perform measurements well below the crests of the waves. The observation heights can be expressed as a dimensionless height k_pz, where k_p is the wavenumber of the dominant waves. For PA1, k_pz ranged between 0.048 and 0.098, for PA2 between 0.095 and 0.19, and for GS between 0.22 and 0.45.

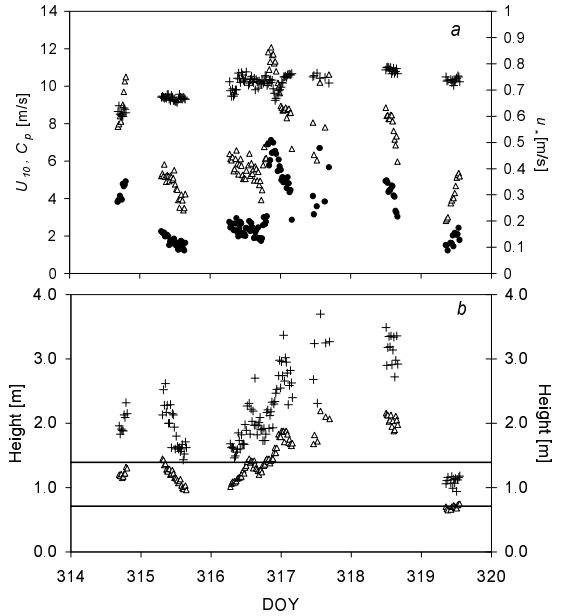

Figure 2. a) U_{10}, C_p (left axis; triangles and pluses, respectively) and u_* (right axis; dots) during the WF experiment; b) H_s (triangles), H_{max} (pluses) and levels of PA1 and PA2 (lower and upper solid line, respectively).

The first step in the data processing is the correction of w. This was done using the position information of the wave follower as well as the velocity derived from readings of the accelerometers integrated in the WF. Both methods yield virtually the same results. The average w after correction is in general less than 1 cm/s. In the EC processing software, we subsequently apply a standard tilt correction to reduce it to zero.

The next step is to extract the wave-coherent signals from the timeseries. We applied the method proposed by Hristov *et al*. (1999). This method is based on a spectral analysis of the data by means of the Hilbert transform. It was developed especially to compute phase-locked averages over non-monochromatic wave fields. First, a phase averaged surface elevation, $\tilde{\eta}$, is computed. This defines an "average wave", serving as a reference framework for the phase-averaged velocities. We fitted 5th-order

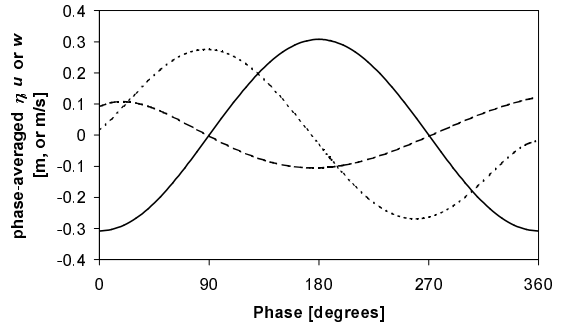

Figure 3. Example of $\tilde{\eta}, \tilde{w}$ and $\tilde{u}$ (solid line, dotted line and dashed line, respectively).

polynomials to describe the phase-locked signals. An example of $\tilde{\eta}, \tilde{w}$ and $\tilde{u}$ from PA1 is given in Fig. 3. For the particular case shown, U_{10} = 4.0 m/s, H_s = 1.03 m and C_p = 9.4 m/s. The average wave, represented by $\tilde{\eta}$, moves from the right to the left. The $\tilde{w}$ pattern is observed in all cases and for all instruments, though with smaller amplitude at higher levels and smaller wave heights, and reflects that air is pushed up upon the approach of a wave. In this example the pattern of $\tilde{u}$ suggests that air slows down over the wave crests, and speeds up in the troughs. In other runs, however, we see the opposite behavior.

The wave-induced momentum fluxes $\tilde{u}\tilde{w}$ and $\tilde{v}\tilde{w}$ were computed from the fitted functions. The total wave-induced stress

$$u_w^2 \equiv \sqrt{\left(\overline{\tilde{u}\tilde{w}}\right)^2 + \left(\overline{\tilde{v}\tilde{w}}\right)^2} \quad , \qquad (4)$$

also defines a wave-coherent velocity scale u_w. The normalized wave-induced stress $(u_w/u_*)^2$ is shown in Fig. 4a for PA1, PA2 and GS. The timeseries are smoothed with a 7-point running-mean filter. The data reveal a correlation between the wave-induced fluxes and C_p/u_*. Due to the normalization, some correlation is expected. However, we found u_w^2 to be correlated with *inverse* wave age u_*/C_p (not shown). These results confirm that wave age can be used in scaling problems of the WBL, as suggested by Hare *et al.* (1997). The stress partitioning ratio $(u_w/u_*)^2$ varies between 0.05 and 0.25 for both PA1 and PA2, and between 0.01 and 0.1 for GS. The ratios of u_w^2 from PA2/PA1 and GS/PA1 (Fig. 4b) suggest that u_w^2 at the level of GS is, typically, 40% of the one at the level of

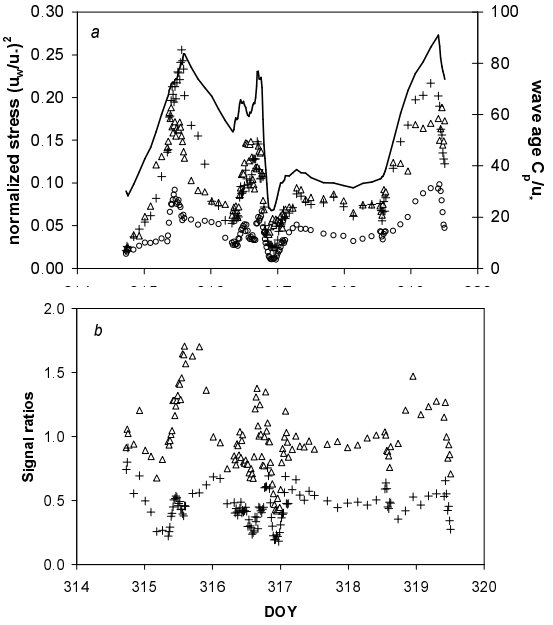

Figure 4. a) Smoothed timeseries of $(u_w/u_*)^2$ (left axis; PA1 (triangles), PA2 (pluses) and GS (dots)) and C_p/u_* (right axis; solid line); b) ratio of u_w from PA2/PA1 (triangles) and GS/PA1 (pluses).

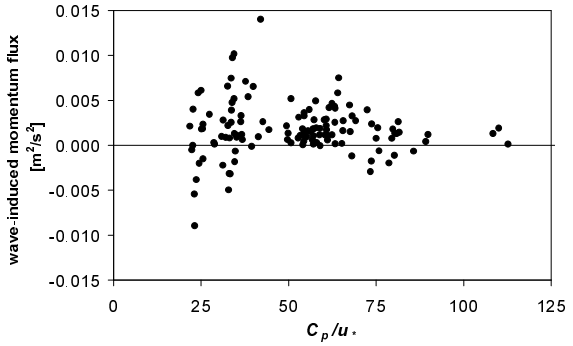

Figure 5. Wave-induced momentum transport versus wave-age (from PA1).

PA1. At the level of PA2, u_w^2 is typically 90-100% of the one at PA1. However, in both cases large changes in the signal ratios occur, and at the level of PA2, u_w^2 may also be larger than at the lower level. We can now make a rough evaluation of vertical decay length scales, as discussed in, e.g., Makin and Kudryavtsev (1999). Potential flow theory predicts an exp(-2*kz*) vertical decay function for wave-induced fluxes. Then, taking $k=k_p$, we expect u_w^2 ratios of about 0.8-0.9 for PA2/PA1, and 0.5-0.65 for GS/PA1. Using the phase speed of the average wave improves the prediction for the lower level. Rapid distortion theory suggests the so-called inner region height L_i, as the decay length, so that the wave-induced momentum flux decays as exp(-z/L_i). L_i is defined by $kL_i=2\kappa u_*/|U_L-c|$ (where κ=0.4 is the von Kármán constant, U_L is the wind speed at L_i, and c is the phase speed of waves with wavenumber k). We computed k_pL_i with $c=C_p$, and found L_i in most cases to be only 25-50% of the level of PA1 (71 cm). With this decay length scale, signal ratios would be far below the observed ones.

Finally, we computed the component of u_w^2 aligned with the travelling direction of the dominant waves. Fig. 5 depicts results from PA1 versus C_p/u_*. The data show the following tendency: 1) a negative flux at low C_p/u_*, when the waves absorb momentum to grow; 2) a positive flux at intermediate C_p/u_*, when the waves deliver momentum to the air; 3) hardly any interaction at very high C_p/u_*, suggesting that the air smoothly follows the surface (see Grachev and Fairall, 2001, for a more thorough discussion of these tendencies). Unfortunately, our results do not include very young seas, which prevents drawing definite conclusions in this respect. Also, they are more scattered than those from Hristov *et al*. (1999), which may be due to the many occurrences of mixed seas during the experiment.

4. CONCLUDING REMARKS AND OUTLOOK

In the present contribution we described our specialized WF, mounted with pressure anemometers to perform EC measurements of momentum fluxes within the WBL at sea, in wave-following co-ordinates, and below the level of the wave crests. During a field experiment in November 2001, all instruments functioned reliably. A first analysis of the data shows that we can extract valuable information on the structure of the WBL at sea. In the future, we will refine and extend the present analyses and procedures to obtain more detailed information on wave-coherent turbulence. Video images will support such analysis, e.g., to assess the influence of breaking waves. We will test existing WBL theories and predictions from numerical simulations. In subsequent field programs we plan to extend the measurement program, for example by observing static pressure fluctuations.

REFERENCES

Bye, J., V. Makin, A. Jenkins and N.E. Huang, 2001: Coupling mechanisms. In: I.S.F. Jones and Y. Toba (Eds.), *Wind Stress over the Ocean*, Cambridge University Press, Cambrigde, 142-154.

Finnigan, J.J., F Einaudi and D. Fua, 1984: The interaction betweenan internal gravity wave and turbulence in the stably-stratified nocturnal boundary layer. *J. Atmos. Sci.*, **41**, 2409-2436.

Grachev, A.A., and C.W. Fairall, 2001: Upward momentum transfer in the marine boundary layer. *J. Phys. Oceanogr.*, **31**, 1698-1710.

Hare, J.E., T. Hara, J.B. Edson and J.M. Wilczak, 1997: A similarity analysis of the structure of airflow over surface waves. *J. Phys. Oceanogr.*, **27**, 1018-1037.

Hristov, T., C. Friehe, S. Miller, J. Edson and S. Wetzel, 1999: Structure in the atmospheric surface layer over open ocean waves: representation in terms of phase averages. In: *S.G. Sajjadi, N.H. Thomas and J.C.R. Hunt (Eds.), Wind over wave couplings, perspectives and prospects,* Clarendon Press, Oxford, 99-105.

Kraan, C., and W.A. Oost, 1988: A new way of anemometer calibration and its application to a sonic anemometer. *J. Atmos. Oceanic Tech.,* **6**, 516-524.

Makin, V.K. and V.N. Kudryavtsev, 1999: Dynamical coupling of surface waves with the atmosphere. In: G.L. Geernaert (Ed.): *Air-sea exchange. Physics, chemistry and dynamics*. Kluwer Academic Publishers, Dordrecht, 73-125.

Oost, W.A., E.H.W. Worrell, J.W. Schaap, C. van Oort and C. Kraan, 1991: An improved version of the pressure anemometer. *J. Atmos. Oceanic Tech.*, **8**, 575-584.

Wilczak, J.M., J.B. Edson, J. Højstrup and T. Hara, 1999: The budget of turbulent kinetic energy in the marine atmospheric surface layer. In: G.L. Geernaert (Ed.)*: Air-sea exchange. Physics, chemistry and dynamics.* Kluwer Academic Publishers, Dordrecht, 153-173.

Young, I.R., 1999: *Wind Generated Ocean Waves*. Elsevier, Amsterdam, 288 pp.